Dynamical systems analysis of spike-adding mechanisms in transient bursts

Jakub Nowacki*, Hinke M. Osinga*, Krasimira Tsaneva-Atanasova*

August 17, 2011

Abstract

Transient bursting behaviour of excitable cells, such as neurons, is a common feature observed experimentally, but theoretically it is not well understood. We analyse a five-dimensional simplified model of after-depolarisation that exhibits transient bursting behaviour when perturbed with a short current injection. Using one-parameter continuation of the perturbed orbit segment formulated as a well-posed boundary value problem, we show that the spike-adding mechanism is a canard-like transition, that has a different character from known mechanisms for periodic burst solutions. The biophysical basis of the model gives a natural time-scale separation, which allows us to explain the spike-adding mechanism using geometric singular perturbation theory, but it does not involve actual bifurcations as for periodic bursts. We show that unstable sheets of the critical manifold of the fast subsystem organise the spike-adding transition and investigate the behaviour of the slow flow on the critical manifold near folds of this manifold. Our analysis shows that the orbit segment during the spike-adding transition includes a fast transition between two saddle-unstable sheets of the slow manifold. We also discuss a different parameter regime, where the presence of additional saddle equilibria of the full system alters the spike-adding mechanism.

Keywords: burst, spike-adding, transient behaviour, dynamical systems, geometric singular perturbation theory.

*Bristol Centre for Applied Nonlinear Mathematics, Department of Engineering Mathematics, University of Bristol, Queen's Building, University Walk, BS8 1TR

1 Introduction

The majority of neuron models are high dimensional and, therefore, are characterised by rich dynamics, which manifest themselves by a variety of different behaviours that can be found within a small parameter range. Such properties have provoked a large number of studies based on dynamical systems theory. Pioneering work by Rinzel in [1] classified the bursting mechanisms using the system decomposition into slow and fast subsystems following the ideas of Geometric Singular Perturbation Theory (GSPT) [2, 3, 4, 5]. Rinzel utilised the bifurcation analysis of the fast subsystem and showed that the burst can be divided into active (spiking) and silent phases, which follow different types of attractors of the fast subsystem. Rinzel also performed a classification of the bursting oscillators based on the structure of the bifurcation diagram of the fast subsystem. Later, Terman [6] used the concept of time-scale separation to study the chaotic spiking that arises in bursting oscillators. He identified bifurcations of the periodic bursting solutions that organise the transitions between different parameter regimes. These studies are primarily for systems with one slow variable; see [7] for an extension to two slow variables and [8] for a summary of these ideas along with new results.

The analysis performed by Izhikevich [9, 10] is a rigorous classification of the bursting mechanisms based on the types of bifurcations of the fast subsystem. This classification is similar in nature to the previous works but puts bifurcations as a main theme of classification and shows many competing mechanisms; see also [11, 12].

The classification of bursting mechanisms, however, does not answer questions about the number of spikes in a particular burst of the same type. Terman [13] analysed transitions between bursting and tonic (continuous) spiking. He recognised the importance of connecting classical slow-fast analysis with full system bifurcation analysis, which is necessary to detect chaos in the system. The study in [13] focusses on chaotic dynamics; see [14, 15, 16] for studies that focus on the spike-adding mechanism directly. The analysis shows that the spike-adding mechanism is formed by a pair of saddle-node bifurcations of periodic orbits of the full system; bursts with different numbers of spikes are, in fact, different periodic attractors of the full system that may coexist only if the number of spikes differs by one [13, 16].

The above examples show, that dynamical systems theory, and GSPT in particular, has been successfully used to explain periodic bursting behaviour. In this paper we analyse the spike-adding mechanism in a transient burst, where the burst takes place due to a brief perturbation and a periodic attractor of the full system does not exist. We use GSPT and numerical continuation methods to study such transient behaviour in a model of hippocampal pyramidal neurons from [17].

The numerical methods that we use to analyse the spike-adding mechanism in a transient burst are based on the continuation of orbit segments as solutions of a two-point boundary value problem (BVP); this approach has already been applied to the bifurcation analysis of periodic orbits, including homoclinic or heteroclinic bifurcations [18], and more recently for the computation of invariant manifolds [19] and so-called critical and slow manifolds in systems with multiple time scales [20, 21]. We divide the system into two separate orbit segments, with and without current injection, which are coupled only by the boundary conditions. This allows us to continue the orbit segments in a chosen parameter to study the behaviour of the model in detail. We complement this continuation with the computation of the two-dimensional *critical manifold* of the fast subsystem, which comprises all the equilibria of the fast subsystem parametrised by two slow variables. The critical manifold is folded and consists of a number of stable and unstable sheets. Moreover, the fast subsystem has families

of periodic orbits that emanate from Hopf bifurcations on the critical manifold, which give rise to the spiking behaviour during a burst. Our analysis shows that during the spike-adding transition, orbit segments trace unstable slow manifolds that lie very close to corresponding unstable sheets of the critical manifold. This canard-like behaviour is very similar to behaviour during a spike-adding transition of a periodic burst, but it does not involve bifurcations, and coexistence of different burst types is not possible here.

As for periodic bursting, a spike-adding transition occurs over an exponentially small parameter interval. Within this exponentially small parameter interval, we find an even smaller parameter interval during which the canard-like orbit segment includes a fast transition from a saddle-unstable to *another saddle-unstable* slow manifold. This phenomenon is similar to so-called fold-initiated canards that have been observed for periodic orbits [22]. To understand this behaviour we study the associated slow flow on the critical manifold and identify the effect of folds and folded singularities on the behaviour of the orbit segment.

Our study concerns the analysis of a spike-adding mechanism where the full system has a unique stable equilibrium that does not undergo any bifurcations. We find that for different values of model parameters, the system can have additional unstable equilibria that alter the nature of the spike-adding mechanism. More precisely, the appearance of two saddle equilibria on the critical manifold suppresses the fold-initiated transition between unstable sheets and changes the behaviour of the orbit segment. We use the analysis of the critical manifold along with the associated slow flow to explain this phenomenon.

This paper is organised as follows; in the next section we present our model of study. In Section 3 we numerically identify the mechanism of spike adding via continuation of the orbit segment. Next, in Section 4 we calculate the critical manifold of the fast subsystem along with the slow flow to explain the transition to bursting. Here, we also investigate the transition between two unstable slow manifolds and the effect of the presence of additional equilibria. Finally, we discuss how the spike-adding mechanism changes with the appearance of additional saddle equilibria of the full system. We end with a discussion in Section 5.

2 The model

We apply our analysis of transient bursts to pyramidal neuron cells from the CA1 and CA3 regions of the hippocampus. A detailed model of such neurons in Hodgkin-Huxley formalism was presented in [17], but for the purpose of this paper, we study a reduced version of this model. The simplified model consists of four ionic currents, namely, fast and slow inward currents, denoted I_{FI} and I_{SI}, respectively, and fast and slow outward currents, denoted I_{FO} and I_{SO}, respectively. Inward currents are responsible for the depolarisation or increase of the membrane potential, whereas outward currents hyperpolarise or decrease the membrane potential and return the cell back to its resting state (a stable equilibrium) [23, 24]. The fast inward current I_{FI} represents the fastest class of spike-generating Na^+- and Ca^{2+}-currents. The rates of change of these currents is usually similar to that of the membrane potential. Therefore, we assume that the gating of I_{FI} is instantaneous [17, 23, 25, 26]. The slow inward current I_{SI} mainly corresponds to the transient T-type Ca^{2+}-current [17, 27, 28, 29] and represents the low-voltage activated currents responsible for shaping the subthreshold behaviour of the model. The fast outward current I_{FO} represents high-voltage activated fast K^+-currents that we base on the delayed rectifier K^+-current [17, 23, 25]. Finally, I_{SO} represents muscarinic-sensitive K^+-current [28, 30, 31], which has an activation rate of the

same order as that of I_{SI}.

We only consider the following variables as dynamic: the membrane potential V, the gating variables m_{SI}, m_{FO} and m_{SO} that govern activation of the respective currents, and the gating variable for inactivation of I_{SI}, which we denote by h_{SI}. Hence, our reduced model is five dimensional and has the form

$$\frac{d\mathbf{u}}{dt} = \frac{d}{dt}\begin{pmatrix} V \\ m_{\mathrm{SI}} \\ m_{\mathrm{FO}} \\ m_{\mathrm{SO}} \\ h_{\mathrm{SI}} \end{pmatrix} = \mathbf{f}(\mathbf{u}, \lambda, I_{\mathrm{app}}) := \begin{pmatrix} f_1(\mathbf{u}, \lambda, I_{\mathrm{app}}) \\ f_2(\mathbf{u}, \lambda) \\ f_3(\mathbf{u}, \lambda) \\ f_4(\mathbf{u}, \lambda) \\ f_5(\mathbf{u}, \lambda) \end{pmatrix}. \tag{1}$$

Here, $\mathbf{u} \in \mathbb{R}^5$ is the non-dimensionalised state vector and I_{app} is an applied current that stimulates (perturbs) the cell model when it is non-zero. We specifically indicate further parameter dependencies with the parameter vector $\lambda \in \mathbb{R}^k$, for some integer $k > 0$; in this paper we primarily focus on how the system depends on the maximal conductances of I_{SI} and I_{FO}, because these parameters are not only important for shaping the ADP and bursting behaviours [17], but they are also most likely to vary between neurons, due to different sizes and numbers of channels in different cells (even among the same types of neurons). The right-hand side of (1) has the specific form that is well known from Hodgkin-Huxley formalism: the dynamics of the membrane potential is organised by the equations for the ionic currents, modelled as

$$\begin{aligned} C_{\mathrm{m}}\frac{dV}{dt} &= -\left(I_{\mathrm{FI}} + I_{\mathrm{SI}} + I_{\mathrm{FO}} + I_{\mathrm{SO}}\right) + I_{\mathrm{app}} \\ &= -\big(g_{\mathrm{FI}}\, m_{\mathrm{FI}_\infty}(V)\,(V - E_{\mathrm{I}}) + g_{\mathrm{SI}}\, m_{\mathrm{SI}}^2\, h_{\mathrm{SI}}\,(V - E_{\mathrm{I}}) \\ &\quad + g_{\mathrm{FO}}\, m_{\mathrm{FO}}\,(V - E_{\mathrm{O}}) + g_{\mathrm{SO}}\, m_{\mathrm{SO}}\,(V - E_{\mathrm{O}})\big) + I_{\mathrm{app}}, \end{aligned} \tag{2}$$

where C_{m} is the membrane capacitance. Here, g_x with $x \in \{\mathrm{FI}, \mathrm{SI}, \mathrm{FO}, \mathrm{SO}\}$ are maximal conductances of the currents and E_{I} and E_{O} are Nerst potentials of the inward and outward currents, respectively. Note that I_{FI} only depends on V, that is, $m_{\mathrm{FI}} = m_{\mathrm{FI}_\infty}(V)$ as defined in (4) below. The dynamics of the gating variables is modelled by

$$\frac{dx}{dt} = \frac{x_\infty(V) - x}{\tau_x}, \quad \text{where } x \in \{m_{\mathrm{SI}}, m_{\mathrm{FO}}, m_{\mathrm{SO}}, h_{\mathrm{SI}}\}; \tag{3}$$

the corresponding activation and inactivation steady-state functions $x_\infty(V)$ of the respective currents, as well as $m_{\mathrm{FI}_\infty}(V)$, are given in Boltzmann form as:

$$x_\infty(V) = \frac{1}{1 + \exp\left(-\frac{V - V_x}{k_x}\right)}. \tag{4}$$

Unless specified otherwise, the default values that we use for the parameters of this simplified model are summarised in Table 1.

Figure 1 illustrates three classes of the responses of the simplified model obtained by changing the maximal conductance g_{SI}. These correspond to cell responses, that are typically observed experimentally. During the simulations, the model is perturbed from its stable equilibrium by a short-current injection whose duration guarantees that the rapidly rising membrane potential will reach and cross its local maximum creating a fully developed spike;

$C_{\mathrm{m}} = 1.0$ $\mu\mathrm{F/cm}^2$		
Inward currents:		
	$E_{\mathrm{I}} = 80.0$ mV	
$g_{\mathrm{FI}} = 2.0$ $\mathrm{mS/cm}^2$	$g_{\mathrm{SI}} = 0.5$ $\mathrm{mS/cm}^2$	
$V_{\mathrm{m_{FI}}} = -25.0$ mV	$V_{\mathrm{m_{SI}}} = -54.0$ mV	$V_{\mathrm{h_{SI}}} = -56.0$ mV
$k_{\mathrm{m_{FI}}} = 5.0$ mV	$k_{\mathrm{m_{SI}}} = 5.0$ mV	$k_{\mathrm{h_{SI}}} = 8.5$ mV
	$\tau_{\mathrm{m_{SI}}} = 3.0$ ms	$\tau_{\mathrm{h_{SI}}} = 20.0$ ms
Outward currents:		
	$E_{\mathrm{O}} = -80.0$ mV	
$g_{\mathrm{FO}} = 9.5$ $\mathrm{mS/cm}^2$	$g_{\mathrm{SO}} = 1.2$ $\mathrm{mS/cm}^2$	
$V_{\mathrm{m_{FO}}} = -6.0$ mV	$V_{\mathrm{m_{SO}}} = -20.0$ mV	
$k_{\mathrm{m_{FO}}} = 11.5$ mV	$k_{\mathrm{m_{SO}}} = 10.0$ mV	
$\tau_{\mathrm{m_{FO}}} = 1.0$ ms	$\tau_{\mathrm{m_{SO}}} = 75.0$ ms	

Table 1: Parameter values for the simplified model (1) as defined in (2)–(4).

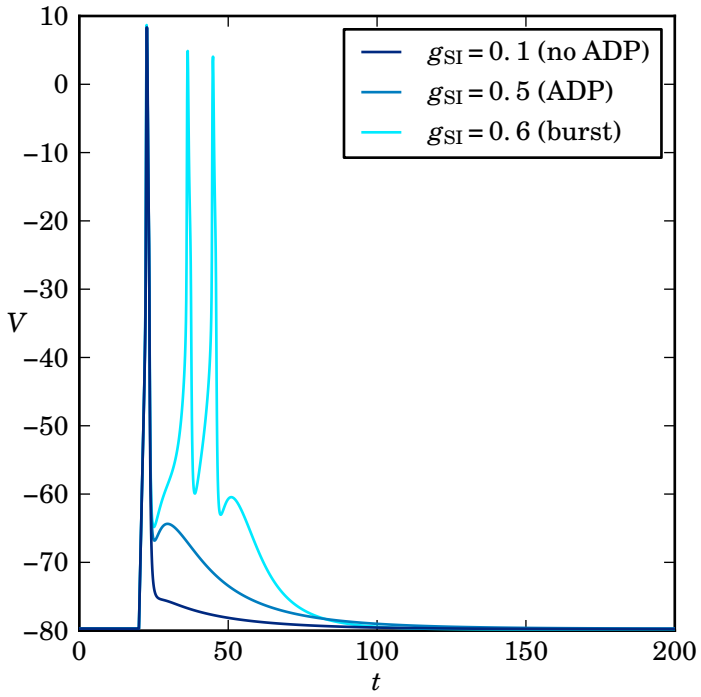

Figure 1: Responses of system (1) to a current injection of $I_{\mathrm{app}} = 20\mu\mathrm{A/cm}^2$ from $t = 50$ to $t = 53$; overlaid are the responses corresponding to different values of the maximal conductance g_{SI} (in $\mathrm{mS/cm}^2$) of the slow inward current, namely, $g_{\mathrm{SI}} = 0.1$, $g_{\mathrm{SI}} = 0.5$ and $g_{\mathrm{SI}} = 0.6$, which are examples of responses with no ADP, with ADP and a (three-spike) burst with ADP, respectively.

see [17, 25, 26, 32] for more details. Two of the three typical responses shown in Figure 1 exhibit a positive deflection of the membrane potential characterised by a 'hump' in the time

trace of the membrane potential at the end of the burst; this is called after-depolarisation (ADP), which can exist, provided $\tau_{m_{\mathrm{FO}}} < \tau_{m_{\mathrm{SI}}}$ [17]. Only the first response (lower curve) is a spike without ADP. Note that the last trace, which corresponds to $g_{\mathrm{SI}} = 0.6$, the highest value of g_{SI} in the example, has sufficiently strong I_{SI} to enable the membrane potential to cross the excitability threshold during the ADP, so that additional spikes are fired.

System (1) defined by equations (2)–(4) evolves on multiple time scales, because C_m/g_{FO} (as an approximation of the time scale for V) and τ_x with $x \in \{m_{\mathrm{SI}}, m_{\mathrm{FO}}, m_{\mathrm{SO}}, h_{\mathrm{SI}}\}$ have different orders of magnitude. As indicated in Table 1, m_{SO} and h_{SI} are slow variables that vary on a time scale that is (roughly) 10 times slower than m_{SI} and m_{FO}, and 100 times slower than V. In particular, this means that our model is capable of firing an arbitrarily large number of spikes during the ADP. More precisely, an increase in g_{SI}, as in Figure 1 and throughout this paper, has the net effect that the slow variable h_{SI} becomes even slower, so that more spikes can be fired during the time it takes for h_{SI} to relax back to its equilibrium value. In this paper we are not interested in the exact nature of this process, but we mention here that a large number of spikes will also be accompanied by a noticeable reduction in oscillation amplitudes, because the dynamics, as h_{SI} slows down, will more and more resemble the behaviour organised by slow passage through a Hopf bifurcation [16, 33]. We focus on the process of spike adding and take advantage of the difference in time scales in Section 3, where we consider the three-dimensional fast subsystem organised by the dynamics of V, m_{SI} and m_{FO}, for which m_{SO} and h_{SI} act as parameters.

The gating variables express the fractions of channels in a given state and naturally range over the interval $[0, 1]$. The natural range of the membrane potential V is bounded by the two Nernst potentials [23, 24], i.e., $E_{\mathrm{O}} \leq V \leq E_{\mathrm{I}}$, where $E_{\mathrm{O}} = -80.0$ mV and $E_{\mathrm{I}} = 80.0$ mV. It is beneficial for the numerical analysis if all variables vary over a similar range. Therefore, the computations are done using the scaled membrane potential V/k_v, where $k_v = 100$ mV. For our numerical investigations, we used the continuation package AUTO [34, 35] for solving the boundary value problems. All numerical simulations were done with XPP [36] using the front-end package XPPy [37] in Python [38] and visualisations were done in Python using Matplotlib [39] and Mayavi [40].

3 Identifying the spike-adding mechanism

Spike adding happens after a current injection, that is, in the regime where $I_{\mathrm{app}} = 0$. Hence, any numerical investigation of the transient behaviour must take into account a discontinuous jump from $I_{\mathrm{app}} > 0$ to $I_{\mathrm{app}} = 0$ on the right-hand side of equation (2). We view the orbit as a concatenation of two orbit segments that are the solution of a two boundary value problems and define appropriate boundary conditions to account for the discontinuity in I_{app}.

More precisely, we consider two successive orbit segments, denoted $\mathbf{u}_{\mathrm{ON}}$ and $\mathbf{u}_{\mathrm{OFF}}$, during which current is injected ($I_{\mathrm{app}} > 0$) and during which it is not ($I_{\mathrm{app}} = 0$), respectively; the concatenation of the two orbit segments $\mathbf{u}_{\mathrm{ON}}$ and $\mathbf{u}_{\mathrm{OFF}}$ gives the orbit segment that characterises the solution of interest. An illustration of this idea is given in Figure 2, where $\mathbf{u}_{\mathrm{ON}}$ is the segment coloured red and $\mathbf{u}_{\mathrm{OFF}}$ the segment coloured blue. Both $\mathbf{u}_{\mathrm{ON}}$ and $\mathbf{u}_{\mathrm{OFF}}$ are solution segments of (1), but for different values of I_{app} and for different integration times T_{ON} and T_{OFF}, respectively. Using the set-up that is standard in AUTO [34, 35], we formulate a boundary value problem using scaled equations, such that the total integration time for

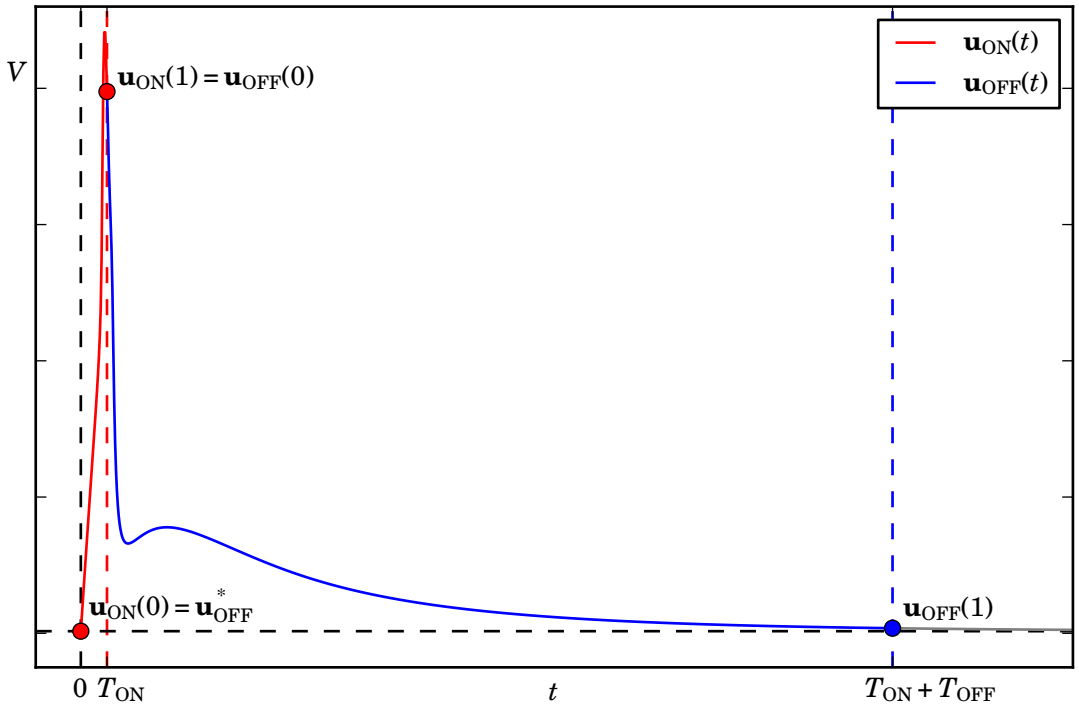

Figure 2: Formulation of system (1) as the boundary value problem (5)–(8). The first (red) segment is the solution $\mathbf{u}_{\mathrm{ON}}(t)$ of (1) with $I_{\mathrm{app}} = 20\mu\mathrm{A/cm}^2$ and $\mathbf{u}_{\mathrm{ON}}(0)$ is at the resting potential $\mathbf{u}^*_{\mathrm{OFF}}$, which is an equilibrium of (1) with $I_{\mathrm{app}} = 0$ (indicated by the horizontal black dashed line); the total integration time is $T_{\mathrm{ON}} = 3\mathrm{ms}$, such that one action potential occurs. The second (blue) segment is the solution $\mathbf{u}_{\mathrm{OFF}}(t)$ of (1) with $I_{\mathrm{app}} = 0$ and $\mathbf{u}_{\mathrm{OFF}}(0) = \mathbf{u}_{\mathrm{ON}}(1)$; the integration time T_{OFF} is fixed to a large enough value so that $\mathbf{u}_{\mathrm{OFF}}(1) \approx \mathbf{u}^*_{\mathrm{OFF}}$.

both segments is 1. That is, $\mathbf{u}_{\mathrm{ON}}$ and $\mathbf{u}_{\mathrm{OFF}}$ are solutions of

$$\mathbf{u}'_{\mathrm{ON}}(t) = T_{\mathrm{ON}}\ \mathbf{f}(\mathbf{u}_{\mathrm{ON}}(t), \lambda, I_{\mathrm{app}}), \tag{5}$$

$$\mathbf{u}'_{\mathrm{OFF}}(t) = T_{\mathrm{OFF}}\, \mathbf{f}(\mathbf{u}_{\mathrm{OFF}}(t), \lambda, 0). \tag{6}$$

In order to obtain a unique solution pair $\{\mathbf{u}_{\mathrm{ON}}, \mathbf{u}_{\mathrm{OFF}}\}$, we must impose boundary conditions. The boundary conditions for (5) are determined by the fact that the current injection perturbs system (1) from its resting potential for a fixed duration T_{ON} as indicated by horizontal black and vertical red dashed lines. Hence, (5) is effectively an initial value problem with $\mathbf{u}_{\mathrm{ON}}(0) = \mathbf{u}^*_{\mathrm{OFF}}$, where $\mathbf{u}^*_{\mathrm{OFF}}$ is the stable equilibrium of (1) with $I_{\mathrm{app}} = 0$; we solve for $\mathbf{u}^*_{\mathrm{OFF}}$ implicitly in AUTO [34, 35] and the boundary condition becomes

$$\mathbf{f}(\mathbf{u}_{\mathrm{ON}}(0), \lambda, 0) = 0. \tag{7}$$

Equations (5) and (7) uniquely define the orbit segment $\mathbf{u}_{\mathrm{ON}}$ as a function of λ for fixed T_{ON}. The orbit segment $\mathbf{u}_{\mathrm{OFF}}$ continues on from $\mathbf{u}_{\mathrm{ON}}$, but now $I_{\mathrm{app}} = 0$. Hence, $\mathbf{u}_{\mathrm{OFF}}$ is again effectively the solution of an initial value problem with initial condition

$$\mathbf{u}_{\mathrm{OFF}}(0) = \mathbf{u}_{\mathrm{ON}}(1). \tag{8}$$

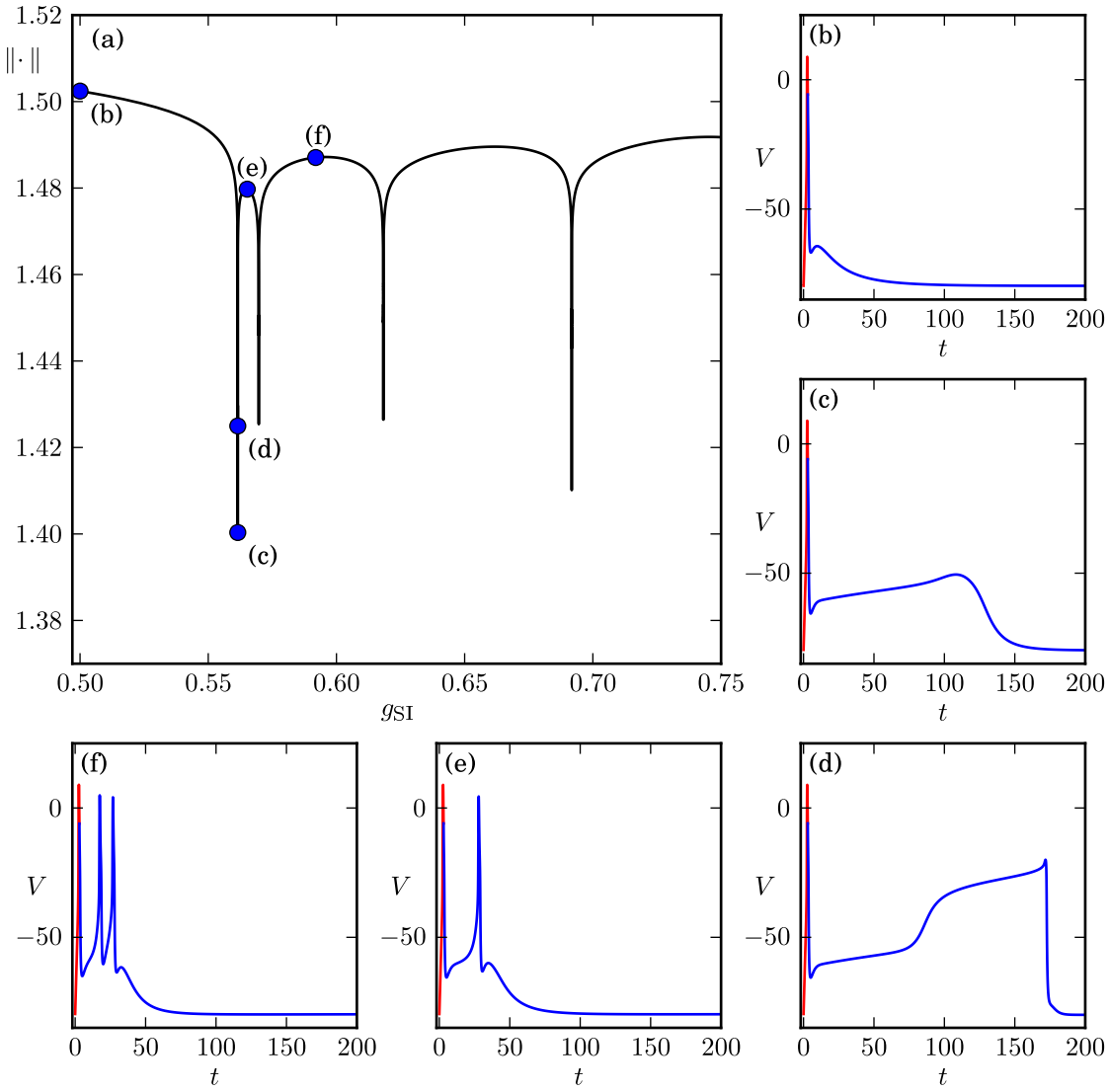

Figure 3: Continuation for increasing g_{SI} of solutions to system (5)–(8); panel (a) shows the AUTO L^2-norm [34, 35] of the solution branch versus g_{SI} and illustrates that the spike-adding mechanism happens suddenly via a pronounced drop in norm; panels (b)–(f) show representative solutions along the branch, indicated by the correspondingly labelled dots in panel (a), and illustrate that solutions during a spike generation, i.e., panels (c) and (d), exhibit a stretched ADP that develops into a double step before relaxing back to the resting potential.

Throughout this paper, we use $I_{app} = 20\,\mu\text{A/cm}^2$ for a total duration $T_{ON} = 3\,\text{ms}$, which is long enough to drive the system past its threshold for the constants as in Table 1. We fix $T_{OFF} = 297\,\text{ms}$ so that the total integration time of the orbit segment is $T_{ON}+T_{OFF} = 300\,\text{ms}$, which is long enough for $\mathbf{u}_{OFF}(1)$ to be (approximately) at the resting potential. System (5)–(8) is now well posed and uniquely defines a λ-dependent solution family.

As illustrated by the example in Figure 1, we expect that increasing g_{SI} leads to a spike-adding transition, namely, a new spike is added on top of ADP when it reaches a critical threshold of the membrane potential V. Hence, we set $\lambda = g_{SI}$ in system (5)–(8) and solve it by continuation in AUTO [34, 35], starting from $g_{SI} = 0.5\,\text{mS/cm}^2$. Figure 3(a) shows the resulting solution branch using the standard L^2-norm of AUTO [34, 35] as a measure. We

observe that the solution norm exhibits a series of fairly constant 'plateaus' that are separated by sharp downward peaks. This behaviour seems similar to that of spike-adding phenomena of periodic bursting solutions, which is organised by pairwise saddle-node bifurcations of periodics [7, 16]. However, our numerical set-up imposes a fixed initial condition, rather than a periodicity contstraint. Hence, uniqueness of solutions of (5)–(8) prevents the possibility of coexisting orbit segments, that is, the branch in Figure 3(a) cannot have folds. The orbit segments of selected solutions along the branch are shown in Figures 3(b)–(f); note that we present the time series up to $t = 200\,\text{ms}$ for clarity of the presentation.

Figure 3(b) shows our starting solution, i.e., a single spike followed by ADP. Along this first plateau of the solution branch up to the first downward peak all orbit segments are qualitatively like Figure 3(b); in particular the ADP is a small hump. As we follow the solutions into the downward peak the hump of the ADP for the orbit segments stretches out as shown in Figure 3(c), which lies at the bottom of the downward peak. Interestingly, as we follow the solution back up along the downward peak, the orbit segment generates a double step in the ADP, as shown in Figure 3(d); we selected the orbit segment with the longest double step (with respect to time). As we continue to trace the solution up along the downward peak, the small spike at the end the orbit segment grows into a fully developed spike, while the stretched double step retracts; the orbit segment shown in Figure 3(e) is representative for such a solution, and all orbit segments along the second plateau in Figure 3(a) are qualitatively like Figure 3(e). Figure 3(f) represents a solution along the next plateau, which exhibits three spikes that are created via the same process as explained above for the two-spike burst. In fact, the same spike-adding process takes place for all spike-adding transitions via the downward peaks in Figure 3(a). This transition from n to $n+1$ spikes in a burst happens over an extremely small parameter interval, during which the solution measure changes rapidly; this suggests that the spike-adding mechanism is organised by the difference in time scales present in system (1). Therefore, in order to obtain a better understanding we proceed by using geometric singular perturbation theory (GSPT) [3, 4, 5, 41, 42, 43].

4 Critical manifold of the fast subsystem

As mentioned in Section 2 the full five-dimensional system (1) contains a three-dimensional fast subsystem with variables V, m_{SI} and m_{FO}. Since m_{SO} and h_{SI} are much slower, the idea of GSPT is to assume that m_{SO} and h_{SI} do not change at all and treat them as parameters. More precisely, we consider the *singular limit* of system (1) and analyse the dynamics of the layer equation

$$\frac{d\mathbf{u}}{dt} = \frac{d}{dt}\begin{pmatrix} V \\ m_{\text{SI}} \\ m_{\text{FO}} \\ m_{\text{SO}} \\ h_{\text{SI}} \end{pmatrix} = \begin{pmatrix} f_1(\mathbf{u}, \lambda, I_{\text{app}}) \\ f_2(\mathbf{u}, \lambda) \\ f_3(\mathbf{u}, \lambda) \\ 0 \\ 0 \end{pmatrix}.$$

Furthermore, because we are interested in spike-adding phenomena *after* the brief current injection, we set $I_{\text{app}} = 0$.

The important objects of study in the singular limit are equilibria and periodic orbits. Since m_{SO} and h_{SI} are parameters, these invariant objects occur in two-parameter families. The $(m_{\text{SO}}, h_{\text{SI}})$-dependent families of equilibria are known as the *critical manifold*, which we denote by S. The equilibria on S can be stable or unstable, determined with respect to

the three-dimensional fast subsystem, and are typically separated by curves of fold or Hopf bifurcations. Similarly, we can expect the existence of $(m_{\rm SO}, h_{\rm SI})$-dependent families P of periodic orbits that emanate from a curve of Hopf bifurcations on the critical manifold; these periodic orbits can again be stable or unstable with respect to the three-dimensional fast subsystem. Typically, the stable periodic orbits of the fast subsystem organise the spiking phase of the bursting oscillators [1, 7, 16].

If $m_{\rm SO}$ and $h_{\rm SI}$ vary slowly enough, then GSPT guarantees that a solution of (1) will trace the $(m_{\rm SO}, h_{\rm SI})$-dependent families of attractors of the fast subsystem [41]. For example, the spikes of system (1) trace the family P^a of attracting periodic orbits of the fast subsystem while $m_{\rm SO}$ and $h_{\rm SI}$ are slowly varying [1, 44]. More precisely, the different sheets of S perturb for the full system (1) to so-called slow manifolds that lie close to S [41]. Solutions of (1) are characterised by fast transitions between, followed by exponential contracion onto the slow manifolds. The essential difference in behaviour during a spike-adding transition is the fact that the solution of (1) contains a segment that traces a slow manifold associated with a sheet of S that is unstable (of saddle type) rather then attracting; see also [3, 5, 15, 43]. While technically the solutions of (1) trace slow manifolds, these lie so close to the critical manifold that we will abuse notation and write 'sheet of S' where we mean 'slow manifold corresponding to the sheet of S.'

The geometry of S and P depends on the values of the other parameters in the system, such as the conductance $g_{\rm SI}$. In order to illustrate the spike generation, we consider the fast subsystem at the fixed value $g_{\rm SI} = 0.5615$ mS/cm^2, which is approximately at the first downward peak in Figure 3(a) where the solution changes from a one-spike to a two-spike transient burst. The critical manifold S for this value of $g_{\rm SI}$ is shown in projection onto $(h_{\rm SI}, m_{\rm SO}, V)$-space from two different viewpoints in Figures 4(a) and (b). The surface was obtained as follows: for ten fixed values of $m_{\rm SO}$ uniformly distributed in the interval $[0, 0.4]$, we computed the $h_{\rm SI}$-dependent curves of equilibria via standard equilibrium continuation with AUTO [34, 35], where we allowed $h_{\rm SI}$ to extend outside its physiological range of $[0, 1]$; the surface S was obtained via concatenation of this collection of ten $m_{\rm SO}$-slices and it is shown in Figure 4 with $h_{\rm SI}$ restricted to the interval $[-1, 1]$ for the sake of presentation.

The critical manifold S in Figure 4 forms a single manifold, containing four fold curves, and can be divided into six different sheets depending on the stability type of the equilibria; the stable sheets are coloured black and the unstable ones red. The bottom (black) sheet is labelled S_1^a and it contains the resting potential as a stable equilibrium on S that is an actual equilibrium of the full five-dimensional system (1) with $I_{\rm app} = 0$. The sheet S_1^a is connected via a curve F_0 of fold bifurcation points to the sheet labelled S_1^r in Figure 4; this fold curve F_0 lies outside $h_{\rm SI} \in [-1, 1]$ and is not shown in Figure 4. The sheet S_1^r is a two-parameter family of equilibria with two stable and one unstable eigenvalues. The next two sheets, labelled S_2^a and S_2^r have the same stability types as S_1^a and S_1^r, respectively; S_2^a is connected to S_1^r via the fold curve F_1 and S_2^a and S_2^r are separated by the fold F_2. The sheet S_3^r is connected to S_2^r via the fold curve F_3 and this sheet consists of equilibria with one stable and two unstable eigenvalues; the two unstable eigenvalues become stable again past the curve H of Hopf bifurcations to form the attracting sheet S_3^a.

The maxima and minima of the families of periodic orbits originating from H are shown in Figures 4(c) and (d), using the same two view points as in panels (a) and (b), respectively. The Hopf bifurcation is subcritical along the entire curve, so that the family is initially unstable (of saddle type), coloured magenta and labelled P^r; the family of periodic orbits becomes stable via a fold of periodic orbits, after which it is coloured blue and labelled P^a, and ends

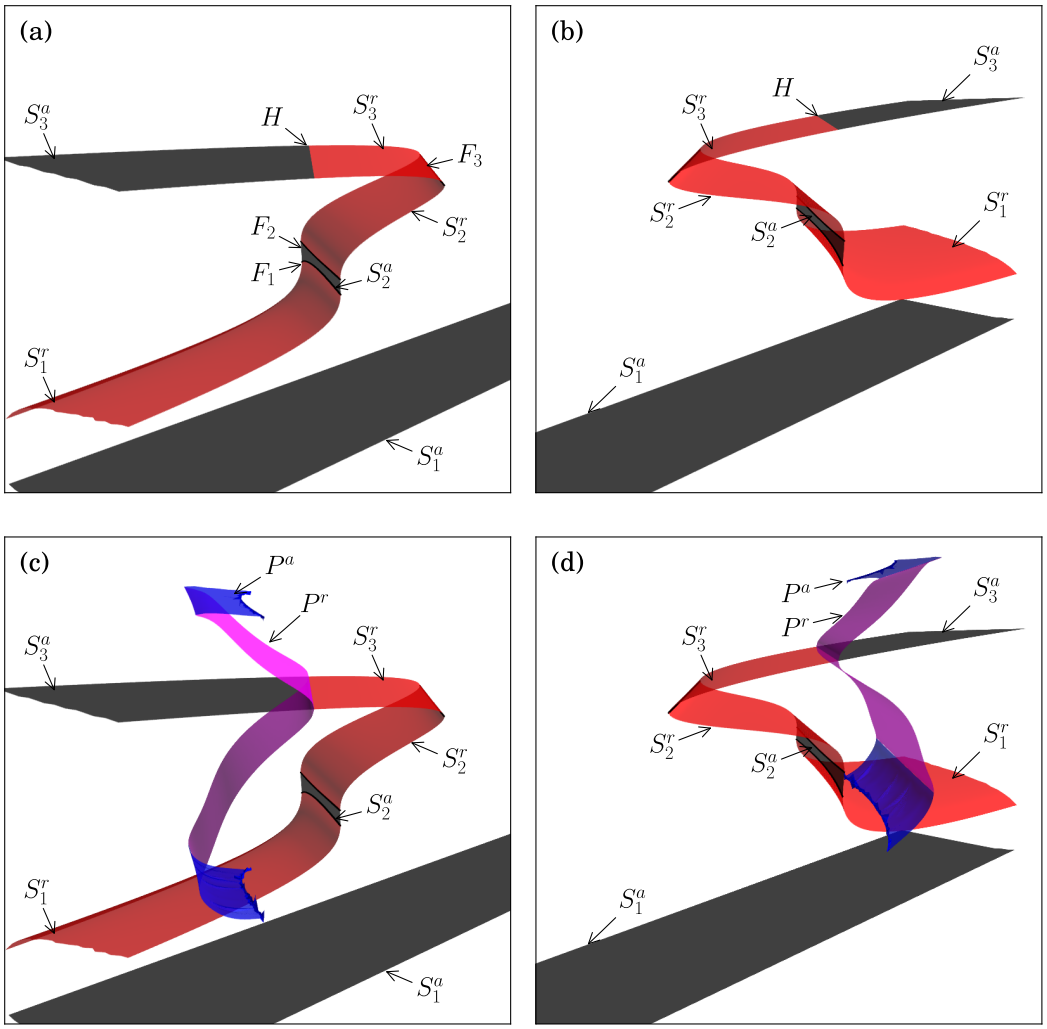

Figure 4: Critical manifolds for $g_{\mathrm{SI}} = 0.5615$ mS/cm^2 projected onto $(h_{\mathrm{SI}}, m_{\mathrm{SO}}, V)$-space of the fast subsystem of (1), where the slow variables m_{SO} and h_{SI} are treated as parameters; panels (a) and (b) show two different view points of the surfaces of equilibria, coloured black when stable and red when not; from the same view points, panels (c) and (d) also show maxima and minima with respect to V of the two-parameter families of periodic orbits, coloured blue when stable and magenta when not. The equilibrium manifold splits into six sheets labelled S_1^a, S_1^r, S_2^a, S_2^r, S_3^r, and S_3^a, that are separated by four fold curves F_0 (not shown), F_1, F_2, and F_3, and a curve of Hopf bifurcations labelled H; the saddle and attracting families of periodic orbits are labelled P^r and P^a, respectively.

in a homoclinic bifurcation involving equilibria on the sheet S_1^r.

Figure 5 illustrates how orbit segments selected from the first downward peak in Figure 3(a), which all correspond to $g_{\mathrm{SI}} \approx 0.5615$ mS/cm^2, trace the different sheets of the critical manifold S for $g_{\mathrm{SI}} = 0.5615$ mS/cm^2; the value of g_{SI} along this downward peak

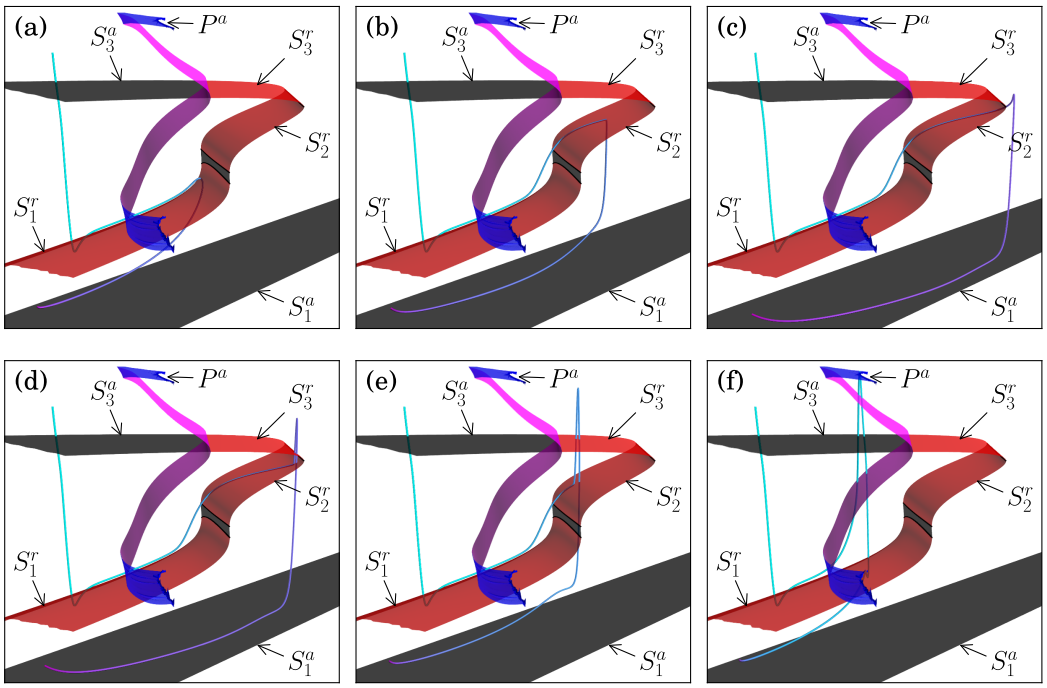

Figure 5: Solutions of system (1) with $g_{\mathrm{SI}} \approx 0.5615$ mS/cm^2 overlayed on the critical manifolds of Figure 4 with $g_{\mathrm{SI}} = 0.5615$ mS/cm^2. The solutions are selected along the first downward peak in Figure 3(a); panel (a) shows a solution just before the minimum of the peak in Figure 3(a) is reached; panel (b) shows one shortly after; panel (c) shows the solutions labelled (d) in Figure 3(a); and panels (d)–(f) show the spike generation as the solution moves up to the next 'plateau' in Figure 3(a).

varies only in the seventh decimal point. For clarity of the presentation we show only the segment $\mathbf{u}_{\mathrm{OFF}}(t)$, that is, after the current injection, depicted as a blue gradient (cyan to magenta) to visualise its evolution in time. In each panel of Figure 5 the orbit segment starts from $\mathbf{u}_{\mathrm{OFF}}(0) = \mathbf{u}_{\mathrm{ON}}(1)$, which is located at the top-left in each panel, above the sheet S_3^a, and traverses the critical manifold S before reaching the stable equilibrium of the full system (1), which lies on the bottom stable sheet S_1^a. As the orbit goes down it seems to pierce through the sheet S_3^a of S, but this is only due to the projection of the critical manifold onto $(h_{\mathrm{SI}}, m_{\mathrm{SO}}, V)$-space; in the full five-dimensional space the orbit segment $\mathbf{u}_{\mathrm{OFF}}(t)$ actually misses S_3^a as it approaches S (and the same applies for the first overshoot near S_1^r).

The transition down and up along the downward peak in Figure 3(a) is characterised by the formation of a stretched ADP, which initially gets increasingly longer, and which shortens again as we follow the solutions along this downward peak. This transition is initiated by the fact that, at the special value $g_{\mathrm{SI}} \approx 0.5615$ mS/cm^2, the injected current perturbs the orbit such that $\mathbf{u}_{\mathrm{ON}}(1) = \mathbf{u}_{\mathrm{OFF}}(0)$ lies almost on the stable manifold of the saddle-unstable sheet S_1^r, so that the orbit segment converges to S_1^r and begins to trace it. Figure 5(a) shows the orbit segment from Figure 3(c), which traces S_1^r almost up to the fold F_1 before it drops down to S_1^a and converges to the resting potential.

Figures 5(b)–(f) illustrate orbit segments for the second upward part of the downward peak in Figure 3(a). Interestingly, a double-step ADP is created via a transition from S_1^r to S_2^r as shown. The longest orbit that was previously shown in Figure 3(d), traces unstable sheets S_1^r to S_2^r of S all the way up to the fold F_3; see Section 4.2 for more details on this robust transition between two saddle-unstable sheets. After reaching the top fold F_3, the membrane potential V initially increases, instead of an immediate decrease down to the stable sheet S_1^a, and a small spike is created. As we continue to follow the solution up along the downward peak, the spike part of the orbit segment grows and moves back towards the attracting periodic orbit family P^a as illustrated in Figure 5(d)–(e). Finally, as shown in Figure 5(f), the orbit segment traces S_1^r for only a very short time before the second spike occurs; this orbit segment is selected almost at the end of the downard peak, after which orbit segments stop tracing S_1^r altogether and the transition from a one- to two-spike transient burst ends.

We remark here that the manner of eventual convergence to the resting potential depends on the nature of the lift-off from the slow manifolds that correspond to the sheets S_1^r or S_2^r. Recall that S_1^r and S_2^r are both sheets of the critical manifold S that consists entirely of saddle equilibria with only one unstable eigenvalue, that is, each point on S_1^r and S_2^r has a one-dimensional repelling fast component. This means that the associated slow manifolds also have a one-dimensional repelling fast component [41]. Hence, orbit segments that trace these saddle slow manifolds can leave it only along a single fast direction. We can see this in Figure 5 as a lift-off from S_1^r 'down' in V, shown in Figure 5(a), or a lift-off from S_1^r 'up' in V, shown in Figure 5(f); this uniquely-defined change in direction along the one-dimensional repelling fast component is real and not just due to the projection onto $(h_{\rm SI}, m_{\rm SO}, V)$-space. The same holds for the sheet S_2^r, for which Figures 5(b) and (e) are good examples that also show the required lift-off 'up' from S_1^r in order to reach S_2^r. In what follows, the notions 'up' and 'down' are with respect to this uniquely-defined change in direction.

The behaviour of the orbit segment of system (1), in relation to the critical manifold S of the fast subsystem that corresponds to the first downward peak in Figure 3(a), is representative for what happens along the other downward peaks in Figure 3(a). Each time when $g_{\rm SI}$ reaches a special value such that the orbit segment comes close enough to the stable manifold of S_1^r, it gets trapped onto S_1^r (or, more precisely, the corresponding saddle slow manifold) for increasingly longer times and the next spike-adding transition begins. Each time, this process includes a transition between two unstable sheets, which organises the double-step ADP solutions. In the next section we first explain the jump at the end of the canard-like behaviour, that is, the behaviour near the fold F_3 that separates the two unstable sheets S_2^r and S_3^r. Section 4.2 discusses the transition between two saddle-unstable sheets, which is a robust part of the spike adding for this example. Section 4.3 illustrates how the spike-adding mechanism can change when additional equilibria are present.

4.1 Slow flow on the critical manifold near F_3

Let us first focus our attention on the behaviour near the fold F_3, that is, the transition from Figure 5(c) to Figure 5(d). The behaviour near folds can be explained by analysis of the slow flow on the critical manifold S [43]. The slow flow on S is defined by the differential algebraic

system

$$\begin{pmatrix} 0 \\ 0 \\ 0 \\ \dot{m}_{\mathrm{SO}} \\ \dot{h}_{\mathrm{SI}} \end{pmatrix} = \begin{pmatrix} f_1(\mathbf{u},\lambda) \\ f_2(\mathbf{u},\lambda) \\ f_3(\mathbf{u},\lambda) \\ f_4(\mathbf{u},\lambda) \\ f_5(\mathbf{u},\lambda) \end{pmatrix}. \tag{9}$$

Here, we always have $I_{\mathrm{app}} = 0$. Recall that the gating variables of (1) are only coupled through the membrane potential V. In fact, it is easy to solve equations $f_2(\mathbf{u},\lambda) = 0$ and $f_3(\mathbf{u},\lambda) = 0$ explicitly, which gives us the solutions for the fast gating variables $m_{\mathrm{SI}} = m_{\mathrm{SI}_\infty}(V)$ and $m_{\mathrm{FO}} = m_{\mathrm{FO}_\infty}(V)$. We substitute these solutions into f_1 to obtain

$$\begin{pmatrix} 0 \\ \dot{m}_{\mathrm{SO}} \\ \dot{h}_{\mathrm{SI}} \end{pmatrix} = \begin{pmatrix} f_1^*(V, m_{\mathrm{SO}}, h_{\mathrm{SI}}, \lambda) \\ f_4^*(V, m_{\mathrm{SO}}, \lambda) \\ f_5^*(V, h_{\mathrm{SI}}, \lambda) \end{pmatrix},$$

that is, the slow flow on the two-dimensional critical manifold S is defined by two ordinary differential equations for m_{SO} and h_{SI} and a single algebraic constraint $f_1^*(V, m_{\mathrm{SO}}, h_{\mathrm{SI}}, \lambda) = 0$. Unfortunately, S is folded with respect to V so that m_{SO} and h_{SI} do not uniquely define V; however, the algebraic constraint does uniquely define m_{SO} or h_{SI} from given pairs (V, m_{SO}) or (V, h_{SI}), respectively; compare also Figure 4(a) and (b). Hence, it is advantageous to express the slow flow in terms of only one of the slow variables m_{SO} or h_{SI} together with the fast variable V.

We choose to work with V and m_{SO}. If we formally differentiate the algebraic constraint we obtain

$$\begin{pmatrix} \dot{V} \\ \dot{m}_{\mathrm{SO}} \end{pmatrix} = \begin{pmatrix} \left[-\frac{\partial f_1^*}{\partial V}\right]^{-1} \left[\frac{\partial f_1^*}{\partial m_{\mathrm{SO}}} f_4^* + \frac{\partial f_1^*}{\partial h_{\mathrm{SI}}} f_5^*\right] \\ f_4^* \end{pmatrix}, \tag{10}$$

where h_{SI} is uniquely determined from $f_1^*(V, m_{\mathrm{SO}}, h_{\mathrm{SI}}, \lambda) = 0$. We refer to [43] for more details on this step. Note that (10) becomes singular when $\partial f_1^*/\partial V = 0$, that is, precisely where S has folds with respect to V. We can desingularise the flow by scaling time with the factor $-\partial f_1^*/\partial V$. This rescaling reverses the direction of the time whenever $\partial f_1^*/\partial V > 0$ and we obtain the desingularised slow flow in the form

$$\begin{pmatrix} \dot{V} \\ \dot{m}_{\mathrm{SO}} \\ 0 \end{pmatrix} = \begin{pmatrix} \frac{\partial f_1^*}{\partial m_{\mathrm{SO}}} f_4^* + \frac{\partial f_1^*}{\partial h_{\mathrm{SI}}} f_5^* \\ -\frac{\partial f_1^*}{\partial V} f_4^* \\ f_1^* \end{pmatrix}. \tag{11}$$

The actual slow flow on S is now defined by the desingularised slow flow (11), where we must take into account the time reversal in the regimes where $\partial f_1^*/\partial V > 0$. Figure 6 illustrates this for a neighbourhood of the fold F_3 on S that separates the sheets S_2^r and S_3^r; we have $\partial f_1^*/\partial V < 0$ on S_3^r and $\partial f_1^*/\partial V > 0$ on S_2^r. The phase portraits in Figure 6 are projected onto the (m_{SO}, V)-plane. Figure 6(a) shows how a trajectory of (11) near F_3 (grey line) is attracted to a focus equilibrium of the desingularised slow flow, marked with a black dot on F_3. Figure 6(b) shows the corresponding projection of the slow flow (9) on S; note the change in direction of the flow for the region where $\partial f_1^*/\partial V > 0$. The fold F_3 in Figure 6(b) is now divided into two parts, a repelling segment on the left side of the focus equilibrium (light-green line) and an attracting segment on the right side of the focus equilibrium (dark-green

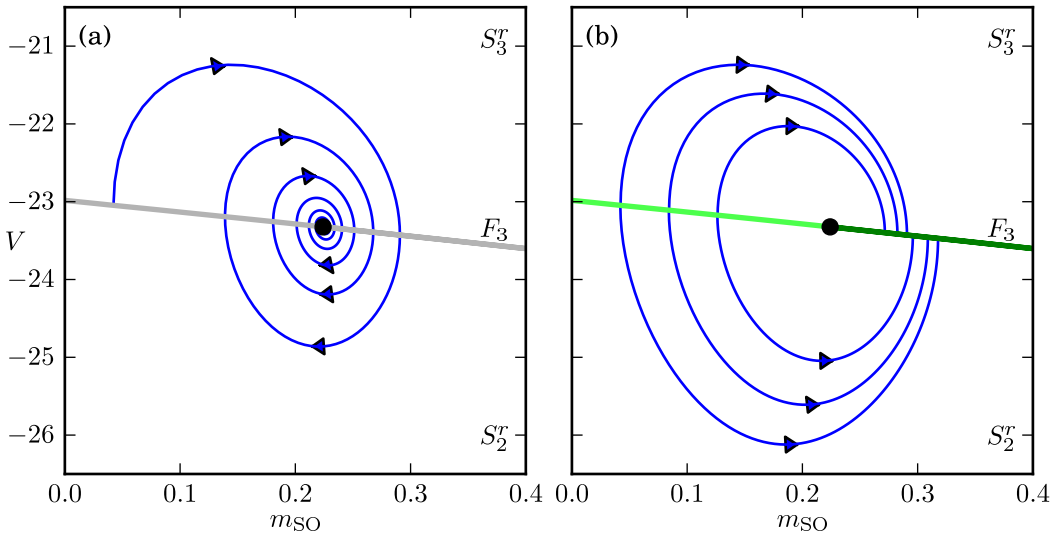

Figure 6: Phase portraits on the sheets S_2^r and S_3^r of the critical manifold S near the fold F_3; panel (a) shows a trajectory of the desingularised slow flow (11), which converges to an attracting focus on F_3 (grey line); panel (b) shows projected trajectories of the slow flow (9); the repelling and attracting nature of F_3 is indicated by light- and dark-green colours, respectively.

line). In fact, the focus equilibrium is no longer a focus; it has become a folded singularity or, more precisely, a folded focus. We refer to [5, 43] for more details. Figure 7 shows a zoom of the sheets S_2^r and S_3^r of the critical manifold near the folded singularity, with the orbit segment from Figure 5(c) depicted by a blue-gradient curve as before. The slow flow is visualised as a vector field on S, where hotter colours depict vectors with a higher magnitude (the length of the vectors is constant for clarity of presentation). The fold F_3 in Figure 7 is coloured the same dark and light green as in Figure 6(b). The inside- and top-view of the critical manifold are presented in Figures 7(a) and (b), respectively.

Figure 7(a) shows that the orbit segment follows the slow flow on S_2^r as it approaches F_3. In a neighbourhood of the folded focus the slow flow has the form of large semi-cycles that cause the orbit segment to trace S_2^r laterally and, at the same time, push it toward F_3. Since the flow on the top sheet S_3^r also points towards F_3 as shown in Figure 7(b), the orbit segment cannot pass F_3 and reaches a so-called jump point; compare also with Figure 6(b). At the jump point, the fast directions of the flow take over, which causes the formation of a small spike as the orbit segment leaves S; see also Figure 5(c). Let us emphasise here that the behaviour of the orbit segments near F_3 does not involve interactions with the slow flow on S_3^r; this impression is given by the projections shown in Figure 5, particularly in panels (d) and (e). As mentioned at the end of Section 4, the spike-formation that develops as soon as an orbit segment has reached F_3 is due to a lift-off 'up' from S_2^r or S_1^r, as in Figure 5(f), and takes place on the fast time scale; the spike and subsequent drop down to S_1^a misses both surfaces S_3^r and S_2^r entirely.

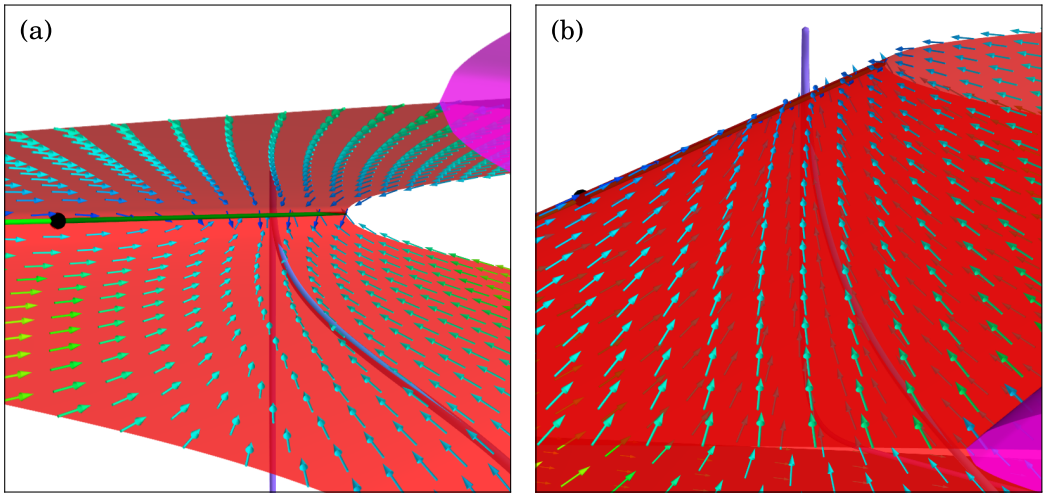

Figure 7: Vectors of the slow flow on S near the top fold F_3 together with the orbit segment from Figure 5(c); the direction of flow on S is indicated by the arrows, where hotter colours correspond to vectors with larger magnitudes. The folded focus is the black dot on F_3, with the uniformly repelling and attracting parts of F_3 coloured light and dark green, respectively. Panels (a) and (b) show the bottom and top views of the process, respectively.

4.2 Slow flow of the critical manifold near the folds F_1 and F_2

The formation of a new well-developed spike occurs over an exponentially small parameter interval $g_{\mathrm{SI}} \approx 0.5615$ mS/cm^2 for which the effect of the injected current is precisely such that the orbit segment comes close to the stable manifold of S_1^r. The behaviour of the orbit segment near the top fold F_3 corresponds to the onset of such a new spike, but the process of reaching F_3, as illustrated in Figures 5(a) and (b), as well as the further development of the spike, as illustrated in Figures 5(d)–(f), involves the creation of a double-step ADP; this behaviour is organised by a (fast) jump from S_1^r to another saddle-unstable sheet S_2^r. Such a jump, which is actually a jump between the two corresponding unstable slow manifolds, is a phenomenon that occurs robustly as part of the spike-adding mechanism and has previously been observed for periodic orbits in planar systems; it was reported as a new type of canard called *fold-initiated canards* in [22] and a slightly different version termed *ducks with relaxation* is discussed in [45, Ch. 4, Sec. 5.4].

In this section we focus on the creation of the double-step ADP, which is organised by the slow flow on S near F_1 and F_2; see Figures 5(a) and (b). This transition is illustrated in Figure 8. Figure 8(a) shows the same orbit segment as in Figure 5(a), and Figures 8(b) and (c) show two subsequent orbit segments that both occur before the case shown in Figure 5(b). As before, the orbit segments are depicted as blue-gradient curves and the colour-coded vectors indicate the slow flow on S. We observe that the orbit segment in Figure 8(a) exhibits a lift-off down from S_1^r before a fast jump down to S_1^a returns the system to its resting potential, while the two orbit segments in Figures 8(b) and (c) exhibit a lift-off up from S_1^r.

In fact, within the exponentially small parameter interval during which a spike is added, we can continuously parametrise the entire family of orbit segments by the moment of lift-off

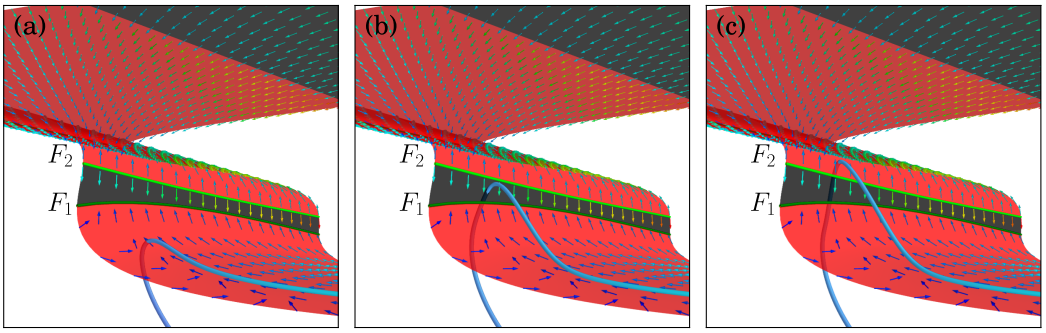

Figure 8: Vectors of the slow flow on S in the vicinity of the two folds F_1 and F_2 that mark the transition of the orbit segment between the two unstable sheets S_1^r and S_2^r; the direction of flow on S is indicated by the arrows, where hotter colours correspond to vectors with larger magnitudes. The attracting fold F_1 is dark green and the repelling fold F_2 is light green. Panels (a)–(c) show the same perspective with orbit segments that almost reach F_1, reach F_1 via the attracting sheet S_2^a, and reach F_2 with a jump from S_1^r to S_2^r, respectively.

(first down and then up) from S_1^r. At the start of the spike-adding process, orbit segments trace only the saddle-unstable sheet S_1^r before a lift-off down to S_1^a returns the system to its resting potential; the example in Figure 8(a) shows an orbit segment that almost reaches F_1. As $g_{\mathrm{SI}} \approx 0.5615$ mS/cm^2 increases continuously (but only exponentially small), the orbit segments come increasingly closer to S_1^r until one actually reaches F_1; these orbit segments grow increasingly longer stretched ADPs.

Using the analysis via the desingularised slow flow (11) as derived in Section 4.1, we can decide what happens when an orbit segment reaches F_1. We find that the desingularised slow flow (11) does not have any equilibria in the neighbourhood of the two folds F_1 and F_2, which means that there are no folded singularities on either F_1 or F_2; the fold curve F_1 is uniformly attracting, which we indicated by a dark-green colour, and F_2 is uniformly repelling, indicated by a light-green colour. Hence, upon reaching F_1, the orbit segment simply jumps down toward the resting potential and subsequent orbit segments exhibit a lift-off up from S_1^r. Since the sheet S_2^a on the other side of F_1 is attracting, the fast directions will push these orbit segments toward S_2^a. Note that the slow flow on S_2^a points back to F_1, so these orbit segments will flow to F_1 from the other side and drop down to S_1^a that way; an example is shown in Figure 8(b).

Since there are no folded singularities on the folds F_1 and F_2, each fold point has the same effect on the dynamics. Furthermore, the repelling fast component is one dimensional in this neighborhood of the phase space, which means that the dynamics here is essentially planar and behaves in the same way as the example discussed in [22]. As we continue to increase $g_{\mathrm{SI}} \approx 0.5615$ mS/cm^2 ever so slightly, orbit segments will converge to S_2^a closer and closer near F_2, until the lift-off up from S_1^r happens far enough from F_1 such that they may reach F_2. This marks the start of a (doubly) exponentially small parameter regime of the fold-initiated canard behaviour [22] within the family of spike-adding orbit segments. Since F_2 is uniformly repelling, the slow flow pushes an orbit segment that comes close enough to F_2 onto S_2^r and away from F_2, resulting in the double-step ADP as part of the spike-adding transition. We stress that most orbit segments within the exponentially small parameter

range $g_{\mathrm{SI}} \approx 0.5615$ mS/cm^2 that exhibit a lift-off up from S_1^r miss F_2 altogether and form a well-developed spike as illustrated in Figure 5(f).

4.3 Spike adding when additional equilibria are present

It turns out that the spike-adding mechanism organised by canard-like behaviour during the downward peaks of Figure 3(a) always features a double-step ADP stage involving a jump between S_1^r and S_2^r. Hence, each downward peak in Figure 3(a) corresponds to a qualitatively similar transition as discussed for the first one at $g_{\mathrm{SI}} \approx 0.5615$ mS/cm^2. If we increase g_{FO} from the fixed value $g_{\mathrm{FO}} = 9.5\,\mathrm{mS/cm^2}$ that was used in Figure 3 to the new value $g_{\mathrm{FO}} = 9.6\,\mathrm{mS/cm^2}$ then the nature of spike adding changes due to the presence of additional unstable equilibria of system (1). If we again continue the two-point boundary value problem (5)–(8) as before with $\lambda = g_{\mathrm{SI}}$, but $g_{\mathrm{FO}} = 9.6\,\mathrm{mS/cm^2}$ set to its new value, we get a bifurcation diagram similar to the one for $g_{\mathrm{FO}} = 9.5\,\mathrm{mS/cm^2}$ shown in Figure 3. In fact, the spike-adding mechanism for the first four additional spikes involves a double-step ADP stage as we have seen in the previous section. However, for $g_{\mathrm{SI}} \approx 0.7672$ mS/cm^2, that is, just before the transition from five to six spikes, a saddle-node bifurcation occurs on the saddle-unstable sheet S_1^r. This creation of two new (unstable) equilibria prevents a double-step ADP stage; the spike-adding mechanism only involves orbit segments exhibiting a stretched ADP with a singe step and there is no longer a jump between unstable slow manifolds.

Let us focus on the transition from a burst with five to one with six spikes, which takes place at $g_{\mathrm{SI}} \approx 0.7842\,\mathrm{mS/cm^2}$. For this value of g_{SI} there exists three equilibria, but only one is stable so that there is no bistability. The stable equilibrium is the resting potential on S_1^a. The other two equilibria are saddles, one with one and one with two unstable eigenvalues, denoted s_1 and s_2 respectively; these additional saddle equilibria are located on S_1^r. We calculate the critical manifold S of the fast subsystem for $g_{\mathrm{SI}} = 0.7842\,\mathrm{mS/cm^2}$; it is shown in Figure 9 projected onto $(h_{\mathrm{SI}}, m_{\mathrm{SO}}, V)$-space. Figure 9 illustrates that the critical manifold does not change qualitatively for higher values of g_{FO} and g_{SI}; compare with Figure 4. Two orbit segments, one selected from the falling slope and one from the rising slope of the downward peak at $g_{\mathrm{SI}} \approx 0.7842\,\mathrm{mS/cm^2}$ are superimposed onto S; see Figures 9(a) and (b), with enlargements in Figures 9(c) and (d), respectively. As before, only the part of the orbit segments that starts after the current injection is shown, so only the downward part of the first of the five spikes is visible. The enlargements in Figures 9(c) and (d) also show the slow flow on S in a neighbourhood of the two equilibria, and better visualise the interaction of the two orbit segments with s_1 and s_2. The equilibria s_1 and s_2 are both saddles, but with respect to the slow flow on S, the equilibrium s_1 is stable (black dot) and s_2 is a saddle (red dot).

The value $g_{\mathrm{SI}} \approx 0.7842\,\mathrm{mS/cm^2}$ for this case with $g_{\mathrm{FO}} = 9.6\,\mathrm{mS/cm^2}$ is again special because at the end of the oscillations, when the orbit segment reaches the family of homoclinic orbits where P^a ends, it lies extremely close to the stable manifold of S_1^r so that it drops down and traces the unstable sheet S_1^r of S. The difference with the spike-adding mechanism illustrated in Figure 5 is that the behaviour of the orbit segment on S_1^r is affected by the presence of the equilibria s_1 and s_2. With respect to the two-dimensional slow flow on S_1^r, the equilibrium s_1 is an attractor and all orbit segments on S_1^r converge to s_1, provided they lie in its basin of attraction, which is bounded by the one-dimensional stable manifold of the saddle s_2. In terms of the full five-dimensional flow, S_1^r is obviously repelling, and orbit segments that come close enough to S_1^r will behave according to the slow flow for only a

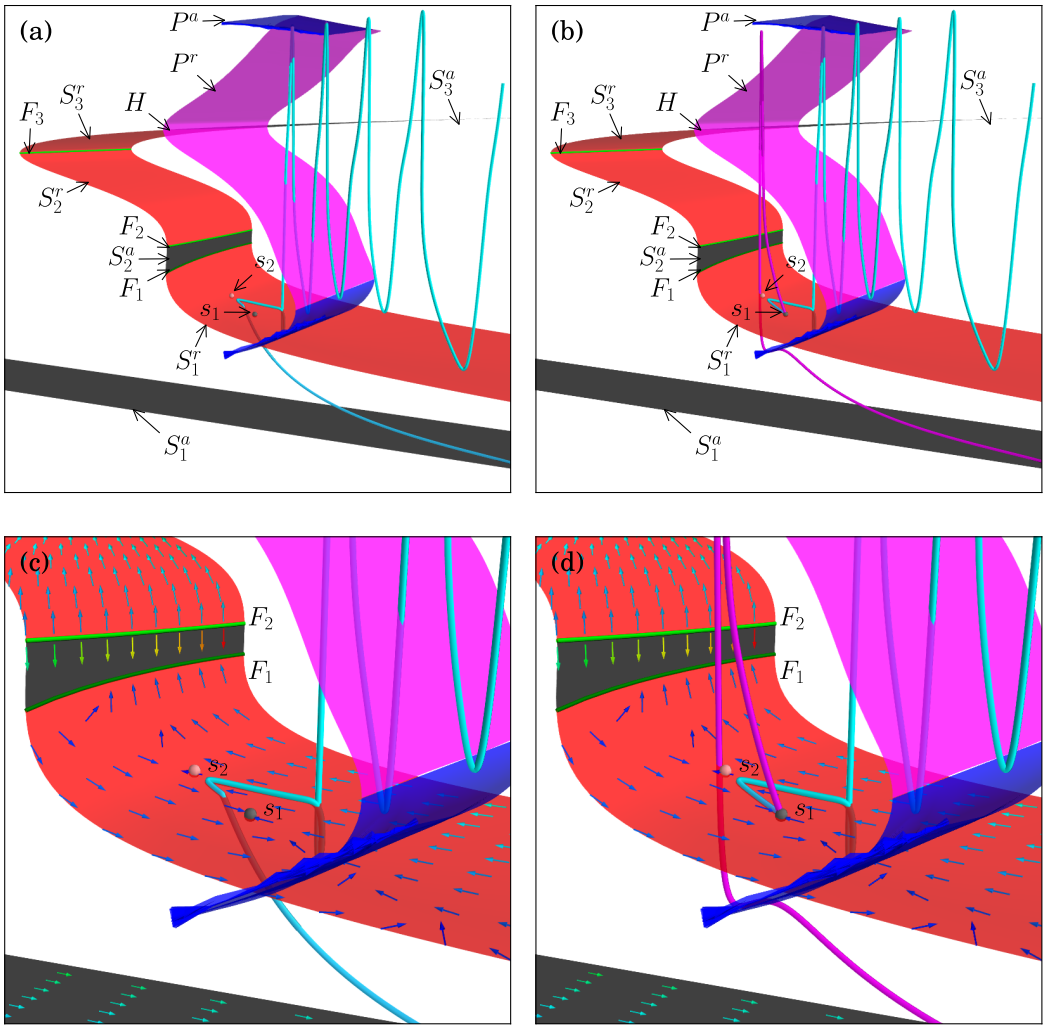

Figure 9: The critical manifold calculated for $g_{\mathrm{FO}} = 9.6\,\mathrm{mS/cm^2}$ and $g_{\mathrm{SI}} = 0.7842\,\mathrm{mS/cm^2}$ projected onto $(h_{\mathrm{SI}}, m_{\mathrm{SO}}, V)$-space; superimposed in the left and right column are orbit segments with $g_{\mathrm{SI}} \approx 0.7842$ selected from the falling and rising slopes of the downward peak, respectively. Panels (a) and (b) show and overall view and panels (c) and (d) enlargements near F_1 and F_2 along with the associated slow flow. The two unstable equilibria s_1 and s_2 of the full system are marked with black and red dots, because they are an attractor and a saddle on S_1^r, respectively.

finite amount of time; this means that convergence to s_1 will eventually be followed by a fast repulsion away from S_1^r. The orbit segment in Figures 9(a) and (c) enters a close enough neighbourhood of S_1^r in the region of the basin of attraction of s_1; hence, for the time that it is following the slow flow, it converges to s_1, but we can clearly see in Figure 9(c) that the fast directions take over before it reaches s_1. Since this orbit segment was selected from the

falling slope of the downward peak of the spike-adding mechanism, the orbit segment jumps straight down toward S_1^a, where it converges to the resting potential. Orbit segments on this slope that lie closer to the minimum of the downward peak would reach s_1, but still jump down toward S_1^a when the fast directions take over. On the other hand, orbit segments from the rising slope of the downward peak eventually experience a lift-off 'up' from S_1^r, so that a large action potential occurs before converging back to the resting potential; this change of direction corresponds to the onset of a new spike, which is more dramatic and abrupt than the gradual increase in V followed by a small-amplitude spike as illustrated in Figure 5. Continuity of the vector field (1) implies that there exists an orbit segment that actually converges to the saddle s_1 and never relaxes back to the resting potential.

We remark here that the presence of additional equilibria such as s_1 and s_2 in the example discussed only affects the spike-adding mechanism if the orbit segments that trace S_1^r enter the basin of attraction of s_1. If such orbit segments trace S_1^r on the other side of the stable manifold of s_2, then a double-step ADP stage would occur. We know from our further model analysis (not shown) that the unstable equilibria persists for higher values of g_{SI} as well as g_{FO}, and in all cases that we investigated, these additional equilibria on S_1^r affect the spike generation in the way as described above.

5 Discussion

In this paper we performed a detailed analysis of the mechanisms of spike generation and spike adding in a transient burst. Based on a reduction of our previous model presented in [17], we identify these mechanisms using numerical continuation of orbit segments that are solutions to a well-posed boundary value problem. In our analysis we utilised the separation of time scales in system (1). We calculated the critical manifold S of the fast subsystem, which organises the behaviour of the system. The spike-generation process is characterised by the fact that orbit segments trace unstable slow manifolds that correspond to unstable sheets of S. More precisely, there are two unstable sheets S_1^r and S_2^r on which all points have only a one-dimensional repelling fast component; this means that the lift-off from the associated unstable slow manifolds is characterised by a uniquely-defined direction. The changes in sign of this direction marks the different phases of the spike-adding transition.

By considering the slow flow on S we were able to explain the onset of a spike, as well as the double-step stretched ADP that leads up to it. For the value of $g_{\mathrm{FO}} = 9.5\,\mathrm{mS/cm^2}$ that we considerd, the onset of a spike is organised by the top fold F_3 of S. This fold contains a folded-focus singularity, but it is not accessible and the spikes are due to (regular) jump points. The folds F_1 and F_2 that are involved in the double-step ADP do not contain any folded singularities and they are uniformly attracting and repelling, respectively. Therefore, the first step in the streched ADP ends at a regular jump point. The second step occurs due to a type of fold-initiated canard, because the slow flow points away from F_2; the fold-initiated canard-like behaviour forms a robust part of the spike-adding mechanism that has also been observed for periodic orbits [22].

We found that the nature of the spike-adding mechanism may change if g_{FO} increases slightly. For higher values of g_{FO}, an increase in g_{SI} causes the appearance of two equilibria s_1 and s_2 on S_1^r that form a saddle-node pair with respect to the slow flow. As it turns out, the presence of these equilibria prevents the double-step ADP. Instead, orbit segments that come close to S_1^r during the spike-generation process flow towards the attracting equilibrium s_1

before a lift-off in the fast direction. This means that the onset of a spike is now organised by s_1 rather than the fold F_3 and the stretched ADP involves only a single step. A spike generated by s_1 is dramatically different from one generated by F_3. While both spike-generations happen in an exponentially small parameter interval, the increase in amplitude of a spike generated by F_3 is gradual and should be viewed as a variation of the orbit segment that depends continuously g_{SI}. On the other hand, a spike generated by s_1 is not a continuous variation and a large-amplitude spike appears abruptly as g_{SI} is increased (on an exponentially small scale). The two families, one with and one without the additional spike, are separated by a heteroclinic connection (via a current injection) from the resting potential to the saddle s_1; our numerical method for continuation of the family only gets past this discontinuity because we do not impose relaxation back to the resting potential, but keep T_{OFF} fixed instead.

In theory, it should be possible to observe a double-step ADP as part of the spike-adding transition even when additional equilibria are present. The occurrence of a double-step ADP in this case only depends on whether tracing of S_1^r commences in the basin of attraction of s_1 or not, which is determined by the stable manifold (restricted to S_1^r) of the saddle equilibrium s_2. In our numerical explorations, the orbit segments always commence tracing S_1^r in the basin of attraction of s_1. Hence, we may conclude that g_{FO} and g_{SI} do not have a profound influence on the relative location where orbit segments begin to trace S_1^r during the spike-adding process. However, other parameters of the system may alter this relative location and provoke a double-step ADP even in the presence of additional equilibria. While this observation indicates a challenge for a precise definition of spike-onset in our context, the two different mathematical notions seem to have the same biological effect.

We believe that the canard-like transition involving unstable sheets of the critical manifold lies at the heart of any spike-adding mechanism. The different phases during the transition, however, could be organised by features other than regular jump points and fold-initiated canards. For example, it should be expected that other folded singularities may appear due to variations in the slow flow on S. An investigation of all possibilities remains an interesting and challenging project for future work.

Acknowledgements

The authors thank Pablo Aquirre, Mathieu Desroches, Bernd Krauskopf, John Guckenheimer and Peter De Maesschalck for helpful discussions. JN was supported by grant EP/E032249/1 from the Engineering and Physical Sciences Research Council (EPSRC), HMO by an EPSRC Advanced Research Fellowship grant, and KT-A by EPSRC grant EP/I018638/1.

References

[1] Rinzel J: **A formal classification of bursting mechanisms in excitable systems**. In *International Congress of Mathematicians* 1987:1578–1593.

[2] Jones CKRT: **Geometric singular perturbation theory**. In *Dynamical Systems*, *Volume 1609 of* Lecture Notes in Mathematics, Springer Berlin / Heidelberg 1995:44–118.

[3] Dumortier F: **Techniques in the theory of local bifurcations: Blow-up, normal forms, nilpotent bifurcations, singular perturbations**. In *Bifurcations and Periodic Orbits of Vector Fields*, Kluwer Academic Publishers 1993:19–74.

[4] Szmolyan P, Wechselberger M: **Canards in $\mathbb{R}^3$**. *Journal of Differential Equations* 2001, **177**(2):419–453.

[5] Wechselberger M: **Existence and bifurcation of canards in $\mathbb{R}^3$ in the case of a folded node**. *SIAM Journal on Applied Dynamical Systems* 2005, **4**:101.

[6] Terman DH: **Chaotic spikes arising from a model of bursting in excitable membranes**. *SIAM Journal on Applied Mathematics* 1991, **51**(5):1418–1450.

[7] Smolen P, Terman DH, Rinzel J: **Properties of a bursting model with two slow inhibitory variables**. *SIAM Journal on Applied Mathematics* 1993, **53**(3):861.

[8] Ermentrout GB, Terman DH: *Mathematical Foundations of Neuroscience*, *Volume 35 of* Interdisciplinary Applied Mathematics. New York, NY: Springer New York 2010.

[9] Izhikevich EM: **Neural excitability, spiking and bursting**. *International Journal of Bifurcation and Chaos* 2000, **10**(6):1171–1266.

[10] Izhikevich EM: *Dynamical Systems in Neuroscience: The Geometry of Excitability and Bursting*. The MIT Press 2006.

[11] Golubitsky M, Josić K, Kaper T: **An unfolding theory approach to bursting in fast-slow systems**. In *Global analysis of dynamical systems: Festschrift dedicated to Floris Takens for his 60th birthday*. Edited by Broer H, Krauskopf B, Vegter G, Institute of Physics Publishing 2001:277–308.

[12] Osinga HM, Sherman A, Tsaneva-Atanasova K: **Cross-currents between biology and mathematics on models of bursting**. *Bristol Centre for Applied Nonlinear Mathematics preprint #1737* 2011, [http://hdl.handle.net/1983/1737].

[13] Terman DH: **The transition from bursting to continuous spiking in excitable membrane models**. *Journal of Nonlinear Science* 1992, **2**(2):135–182.

[14] Govaerts W, Dhooge A: **Bifurcation, bursting and spike generation in a neural model**. *International Journal of Bifurcation and Chaos* 2002, **12**(8):1731–1741.

[15] Guckenheimer J, Kuehn C: **Computing slow manifolds of saddle type**. *SIAM Journal on Applied Dynamical Systems* 2009, **8**(3):854.

[16] Tsaneva-Atanasova K, Osinga HM, Rieß T, Sherman A: **Full system bifurcation analysis of endocrine bursting models**. *Journal of Theoretical Biology* 2010, :1133–1146.

[17] Nowacki J, Osinga HM, Brown JT, Randall AD, Tsaneva-Atanasova K: **A unified model of CA1/3 pyramidal cells: An investigation into excitability.** *Progress in Biophysics and Molecular Biology* 2011, **105**(1-2):34–48.

[18] Champneys AR, Kuznetsov YA, Sandstede B: **A numerical toolbox for homoclinic bifurcation analysis**. *Internat. J. Bifur. Chaos Appl. Sci. Engrg.* 1996, **6**(5):867–887.

[19] Krauskopf B, Osinga HM: **Computing invariant manifolds via the continuation of orbit segments**. In *Numerical Continuation Methods for Dynamical Systems: Path Following and Boundary Value Problems*. Edited by Krauskopf B, Osinga HM, Galán-Vioque J, Springer-Verlag 2007:117–154.

[20] Desroches M, Krauskopf B, Osinga HM: **Mixed-mode oscillations and slow manifolds in the self-coupled FitzHugh Nagumo system**. *Chaos* 2008, **18**:015107.

[21] Desroches M, Krauskopf B, Osinga HM: **The geometry of slow manifolds near a folded node**. *SIAM Journal of Applied Dynamical Systems* 2008, **7**:1131–1162.

[22] Guckenheimer JM, Hoffman K, Weckesser W: **Numerical computation of canards**. *International Journal of Bifurcation and Chaos* 2000, **10**(12):2669–2687.

[23] Hodgkin AL, Huxley AF: **A Quantitive descritpion of membrane current and its application to conduction and excitation in nerve**. *Journal of Physiology* 1952, **105**(117):500–544.

[24] Keener JP, Sneyd J: *Mathematical Physiology: Cellular Physiology*. Springer 2008.

[25] Golomb D, Yue C, Yaari Y: **Contribution of persistent Na^+ current and M-type K^+ current to somatic bursting in CA1 pyramidal cells: combined experimental and modeling study**. *Journal of Neurophysiology* 2006, **96**(4):1912–1926.

[26] Yue C, Remy S, Su H, Beck H, Yaari Y: **Proximal persistent Na^+ channels drive spike afterdepolarizations and associated bursting in adult CA1 pyramidal cells**. *Journal of Neuroscience* 2005, **25**(42):9704.

[27] Jaffe DB, Ross WN, Lisman JE, Lasser-Ross N, Miyakawa H, Johnston D: **A model for dendritic Ca^{2+} accumulation in hippocampal pyramidal neurons based on fluorescence imaging measurements**. *Journal of Neurophysiology* 1994, **71**(3):1065–1077.

[28] Yaari Y, Yue C, Su H: **Recruitment of apical dendritic T-type Ca^{2+} channels by backpropagating spikes underlies de novo intrinsic bursting in hippocampal epileptogenesis**. *The Journal of Physiology* 2007, **580**(2):435.

[29] Blackmer T, Kuo SP, Bender KJ, Apostolides PF, Trussell LO: **Dendritic calcium channels and their activation by synaptic signals in auditory coincidence detector neurons**. *Journal of Neurophysiology* 2009, **102**(2):1218–1226.

[30] Yue C, Yaari Y: **KCNQ/M channels control spike afterdepolarization and burst generation in hippocampal neurons**. *Journal of Neuroscience* 2004, **24**(19):4614–4624.

[31] Yue C, Yaari Y: **Axo-somatic and apical dendritic Kv7/M channels differentially regulate the intrinsic excitability of adult rat CA1 pyramidal cells**. *Journal of Neurophysiology* 2006, **95**(6):3480–3495.

[32] Brown JT, Randall AD: **Activity-dependent depression of the spike after-depolarization generates long-lasting intrinsic plasticity in hippocampal CA3 pyramidal neurons**. *The Journal of Physiology* 2009, **587**(6):1265–1281.

[33] Baer SM, Erneux T, Rinzel J: **The slow passage through a Hopf bifurcation: Delay, memory effects, and resonance**. *SIAM Journal on Applied Mathematics* 1989, **49**:55–71.

[34] Doedel EJ: **AUTO: A program for the automatic bifurcation analysis of autonomous systems**. *Congressus Numerantium* 1981, **30**:265–284.

[35] Doedel EJ, Oldeman BE: *AUTO-07P: Continuation and Bifurcation Software for Ordinary Differential Equations*. Concordia University, Montréal 2007, [http://cmvl.cs.concordia.ca/auto/].

[36] Ermentrout GB: *Simulating, Analyzing, and Animating Dynamical Systems: A Guide to XPPAUT for Researchers and Students*. SIAM 2002.

[37] Nowacki J: *XPPy*. University of Bristol 2010, [http://seis.bris.ac.uk/~enxjn/].

[38] Oliphant T: **Python for scientific computing**. *Computing in Science & Engineering* 2007.

[39] Hunter J: **Matplotlib: a 2D graphics environment**. *Computing in Science & Engineering* 2007.

[40] Varoquaux G, Ramachandran P: **Mayavi: Making 3D data visualization reusable**. In *Proceedings of the 7th Python in Science Conference*, SciPy 2008:51–56, [http://hal.archives-ouvertes.fr/docs/00/50/25/48/PDF/full_text.pdf].

[41] Fenichel N: **Geometric singular perturbation theory for ordinary differential equations**. *Journal of Differential Equations* 1979, **31**:53–98.

[42] Hek G: **Geometric singular perturbation theory in biological practice.** *Journal of Mathematical Biology* 2010, **60**(3):347–86.

[43] Desroches M, Guckenheimer JM, Krauskopf B, Kuehn C, Osinga HM, Wechselberger M: **Mixed-mode oscillations with multiple time scales**. *SIAM Review* (in press).

[44] Rinzel J, Ermentrout GB: **Analysis of neural excitability and oscillations**. In *Methods in Neuronal Modelling*, 2nd edition. Edited by Koch C, Sagev I, The MIT Press 1998:251–292.

[45] Arnol′d VI (Ed): *Dynamical Systems V*, *Volume 5 of* Encyclopaedia of Mathematical Sciences. Springer-Verlag 1994.